

Deep Low-rank Prior in Dynamic MR Imaging

Ziwen Ke, Wenqi Huang, Jing Cheng, *Student Member, IEEE*, Zhuoxu Cui, Sen Jia, Haifeng Wang, Xin Liu, Hairong Zheng, *Senior Member, IEEE*, Leslie Ying, *Senior Member, IEEE*, Yanjie Zhu* and Dong Liang*, *Senior Member, IEEE*

arXiv:2006.12090v3 [eess.IV] 6 Jul 2020

Abstract—The deep learning methods have achieved attractive results in dynamic MR imaging. However, all of these methods only utilize the sparse prior of MR images, while the important low-rank (LR) prior of dynamic MR images is not explored, which limits further improvements of dynamic MR reconstruction. In this paper, a learned singular value thresholding (Learned-SVT) operation is proposed to explore deep low-rank prior in dynamic MR imaging to obtain improved reconstruction results. In particular, we propose two novel and distinct schemes to introduce the learnable low-rank prior into deep network architectures in an unrolling manner and a plug-and-play manner respectively. In the unrolling manner, we propose a model-based unrolling sparse and low-rank network for dynamic MR imaging, dubbed SLR-Net. The SLR-Net is defined over a deep network flow graphs, which is unrolled from the iterative procedures in Iterative Shrinkage-Thresholding Algorithm (ISTA) for optimizing a sparse and low-rank based dynamic MRI model. In the plug-and-play manner, we propose a plug-and-play LR network module that can be easily embedded into any other dynamic MR neural networks without changing the network paradigm. To the best of our knowledge, this is the first time that a deep low-rank prior has been applied in dynamic MR imaging. Experimental results show that both of the two schemes can further improve the reconstruction results, no matter qualitatively and quantitatively.

Index Terms—Dynamic MR imaging, Deep learning, Compressed sensing, Low-rank, Model-based network, Plug-and-play low-rank module

I. INTRODUCTION

DYNAMIC MR imaging is of great value in clinical application, due to its ability to reveal both spatial anatomical information and dynamic information simultaneously. However, obtaining dynamic MR images with high spatio-temporal resolutions is very challenging due to the physiological and hardware limitations. In clinical practice, radiologists often need to balance conflicting requirements, such as spatial resolution, temporal resolution, spatial coverage, and contrast-to-noise ratio. Accelerating dynamic MR imaging from incomplete k-space data has generated great research interest to alleviate these conflicts.

*Corresponding author: yj.zhu@siat.ac.cn, dong.liang@siat.ac.cn

Jing Cheng, Sen Jia, Haifeng Wang, Xin Liu, Hairong Zheng, Yanjie Zhu and Dong Liang are with Paul C. Lauterbur Research Center for Biomedical Imaging, Shenzhen Institutes of Advanced Technology, Chinese Academy of Sciences, Shenzhen, China

Ziwen Ke, Wenqi Huang, Zhuoxu Cui and Dong Liang are with Research Center for Medical AI, Shenzhen Institutes of Advanced Technology, Chinese Academy of Sciences, Shenzhen, China

Ziwen Ke and Wenqi Huang are also with Shenzhen College of Advanced Technology, University of Chinese Academy of Sciences, Shenzhen, China

Leslie Ying is with Department of Biomedical Engineering and the Department of Electrical Engineering, The State University of New York, Buffalo, NY, USA

Code will be available at <https://github.com/Keziwen/SLR-Net>

Several methods exploit the sparsity of dynamic data in $x - f$ domain [1–4], which are well-known as compressed sensing MRI (CS-MRI) [5, 6]. For example, k-t SPARSE [7] explored the sparsity of time-varying image by using a wavelet transform along the spatial direction and the Fourier transform along the temporal direction. k-t FOCUSS [8] incorporated the sparseness as a soft-constraint, whereas the conventional basis pursuit or orthogonal matching pursuit impose the constraint as a hard-constraint. k-t ISD [9] iteratively learned and exploited the support knowledge in xf space to improve CS reconstruction. DLTG [10] introduced patch based learning and temporal gradient sparsity for the reconstruction of cardiac cine. PD-ISD [11] divided the image sequences into 3-D overlapping patches, which enforced to be sparsely expressed over an adaptively trained spatio-temporal dictionary. Manifold-learning methods [12, 13] have also been employed to recover dynamic data from highly under-sampled observations. In [12], a kernel principal component analysis was used to learn the manifold described by the principal components of the feature space. In [13], a bi-linear modeling of data manifolds was proposed to exploit local and latent data structures via a sparsity-aware and bi-linear optimization task.

As an extension of CS, low-rank matrix completion has been applied to dynamic MRI [14, 15]. The spatio-temporal correlations of dynamic MR images produced a low-rank matrix by considering each temporal frame as a column of a space-time matrix. By suppressing the singular vectors of the low-rank matrix that correspond to aliasing artifacts, these methods could obtain improved reconstruction results. For example, PS-SPARSE [16] used spatial-spectral sparsity to regularize partial separability model-based reconstruction. k-t SLR [17] posed the joint estimation of the temporal basis functions and the signal as the recovery of a low-rank matrix. L+S [18] separated dynamic MR data into temporally correlated background (L) and dynamic information (S), and the nuclear norm was used to enforce low rank in L and the l_1 norm was used to enforce sparsity in S. These sparse and/or low-rank methods have made great contributions to improving the spatio-temporal resolution of dynamic MR imaging. However, the relatively long reconstruction time and the empirical selection of the regularization parameter limit the clinical application of these methods.

Recently, deep learning based methods have made encouraging achievements in fast MR imaging [19–38]. According to [38], these methods can be divided into two types, namely those that are based on unrolled algorithms [19–26] and those that are not [27–37]. In unrolling-based deep-learning methods, an iterative reconstruction algorithm is unrolled to a deep network in which all free parameters and transforms

can be learned, even data consistency and variable structure [24]. Other methods that are not based on unrolling employ certain standard neural networks to learn the mapping between input (undersampled k-space data or aliased images) and output (clean images). There are mainly three peer-reviewed works for dynamic MR imaging, namely DC-CNN [39], CRNN [40] and DIMENSION [41]. Although there are a number of related works on ArXiv, here we only focus on these three that are peer-reviewed. DC-CNN proposed a deep cascade of convolutional neural networks with interleaved data consistency stages. CRNN simultaneously learned the spatio-temporal dependencies of cardiac image series by modelling the recurrence of the iterative reconstruction stages with recurrent hidden connections. DIMENSION developed a multi-supervised network training technique to simultaneously constrain both the frequency and the spatial domain information to improve the reconstruction accuracy. All three of these methods used networks to perform alternate minimization algorithm to solve a basic MR optimization problem, which contains a data consistent term and a sparse regularization term. However, a large number of works [12, 14, 15, 17, 18] based on low-rank matrix completion have proved that dynamic MR images have a strong low-rank prior, which can be used to improve the reconstruction. Unfortunately, none of the deep learning based methods take advantage of the low-rank prior of dynamic MR images.

In this paper, we explore deep low-rank prior in dynamic MR imaging. In particular, two novel and distinct schemes are proposed, both of which can effectively utilize the low-rank prior of dynamic MR images. Our contributions could be summarized as follows:

- 1) We explore the deep low-rank prior in dynamic MR imaging, which can utilize the sparse and low-rank prior of dynamic MR data simultaneously. Specifically, a learned singular value thresholding (Learned-SVT) operation is proposed to perform the deep low-rank prior. We provide two schemes to introduce the deep low-rank prior into the deep network architectures in an unrolling manner and a plug-and-play manner respectively, both of which can greatly improve the reconstruction results. To the best of our knowledge, this is the first time that a deep low-rank prior has been applied in dynamic MR imaging.
- 2) In the first scheme, we propose a model-based unrolling sparse and low-rank network for dynamic MR imaging, dubbed SLR-Net. The SLR-Net is defined over a deep network flow graphs, which is unrolled from the iterative procedures in Iterative Shrinkage-Thresholding Algorithm (ISTA) for optimizing a sparse and low-rank based dynamic MRI model.
- 3) In the second scheme, we propose a plug-and-play low-rank network module, which can be easily embedded into deep learning models without changing the network paradigm. By embedding this module, any other deep learning methods, such as DC-CNN and CRNN, can easily explore low-rank prior of dynamic MR images to further improve the reconstruction results.

The rest of this paper is organized as follows. Section II

states the background and the proposed methods. Section III summarizes experimental details and the results to demonstrate the effectiveness of the proposed method, while the discussion and conclusions are presented in Section IV and Section V, respectively.

II. METHODOLOGY

A. Background: Alternate Minimization Using Sparsity Prior for Dynamic MRI

The goal of our work is to estimate a sequence of complex-valued MR images $\mathbf{x} \in \mathbb{C}^{N_x N_y N_t}$ from the undersampled k-space measurements $\mathbf{y} \in \mathbb{C}^{N_x N_y N_t}$. This problem is commonly formulated as the following optimization problem:

$$\mathbf{x}^* = \arg \min_{\mathbf{x}} \frac{1}{2} \|\mathbf{Ax} - \mathbf{y}\|_2^2 + \lambda \|\mathbf{Dx}\|_1 \quad (1)$$

Here $\mathbf{A} = \mathbf{PF}$ is the encoding operator, F is a Fourier transform and P is a under-sampling matrix. The first term is the data fidelity, which ensures that the k-space of reconstruction is consistent with the actual measurements. The second term is often referred to as the prior regularization. λ is a regularization parameter. In CS-based methods, \mathbf{D} is usually a sparse prior of \mathbf{x} in some transform domains, e.g. finite difference, wavelet transform and discrete cosine transformation. An auxiliary variable \mathbf{z} , which is constrained to be equal to \mathbf{Dx} , is usually introduced to decouple the fidelity term and the regularisation term as follows:

$$\arg \min_{\mathbf{x}, \mathbf{z}} \frac{1}{2} \|\mathbf{Ax} - \mathbf{y}\|_2^2 + \lambda \|\mathbf{z}\|_1 + \alpha \|\mathbf{Dx} - \mathbf{z}\|_2^2 \quad (2)$$

where α is a penalty parameter. This variable splitting technique can be solved iteratively by applying alternate minimization algorithm:

$$\begin{aligned} \mathbf{z}^{n+1} &= \arg \min_{\mathbf{z}} \lambda \|\mathbf{z}\|_1 + \alpha \|\mathbf{Dx}^{n+1} - \mathbf{z}\|_2^2 \\ \mathbf{x}^{n+1} &= \arg \min_{\mathbf{x}} \frac{1}{2} \|\mathbf{Ax} - \mathbf{y}\|_2^2 + \alpha \|\mathbf{Dx} - \mathbf{z}^n\|_2^2 \end{aligned} \quad (3)$$

The second equation of Eq.3 is often performed by a backfill operation on k-space, which is known as a data consistency (DC) step: for the k-space coefficients that are initially unknown, one use the reconstructed values. For the coefficients that have already been sampled, one correct the predicted k-space with the combination of the actual sampled k-space and the predicted k-space. The formula and more details about DC can be found in [41]. The optimisation process of Eq.3 can be summarized in the following paradigm:

$$\mathbf{z}^0 \rightarrow \mathbf{z}^1 \xrightarrow{DC} \mathbf{x}^1 \rightarrow \dots \rightarrow \mathbf{z}^N \xrightarrow{DC} \mathbf{x}^N \quad (4)$$

where N is the total number of iterations.

Previous deep learning methods for dynamic MR imaging, such as DC-CNN [39], CRNN [40] and DIMENSION [41], unroll the Eq.3 into specific neural networks in a cascaded [39, 41] or recurrent [40] manner. Their network topologies also satisfy the above paradigm. The difference is that DC-CNN and DIMENSION used N cascaded neural networks, CNNs or KI-Net respectively, to learn the N iterations, while CRNN used parameter sharing mechanism to perform recurrent convolutional neural networks to learn the N iterations.

Although the above three deep learning methods have achieved great performance in dynamic MR imaging, they only take advantage of the sparse prior as shown in Eq.1. In recent years, a large number of works [12, 14, 15, 17, 18] based on low-rank matrix completion have proved that dynamic MR images have a strong low-rank prior, which can be used to improve the reconstruction.

B. The First Scheme: The Proposed Unrolling Network

Regularized matrix recovery or low-rank matrix completion, exploits the compact signal representation in the Karhunen Louve Transform (KLT) domain [14, 15, 17, 42, 43]. Different from Eq.1, which only uses the sparse prior of dynamic image, we introduce the low-rank prior into dynamic MR model and obtain the following optimization problem:

$$\mathbf{x}^* = \arg \min_{\mathbf{x}} \frac{1}{2} \|\mathbf{Ax} - \mathbf{y}\|_2^2 + \lambda_1 \|\mathbf{Dx}\|_1 + \lambda_2 \|\mathbf{x}\|_* \quad (5)$$

where $\|\mathbf{x}\|_*$ is the nuclear norm, which is the sum of the singular values of \mathbf{x} ($\|\mathbf{x}\|_* = \sum_i (\mathbf{\Sigma}_i, i)$, $\mathbf{x} = \mathbf{U}\mathbf{\Sigma}\mathbf{V}^*$). The regularized matrix recovery using nuclear norm minimization has been rigorously studied [44–46]. Next, we will demonstrate how to solve Eq.5 using ISTA solver [47].

By introducing auxiliary variable \mathbf{t} , the fidelity term with the sparse regularisation term and the low-rank regularisation term can be decoupled:

$$\arg \min_{\mathbf{x}, \mathbf{t}} \frac{1}{2} \|\mathbf{Ax} - \mathbf{y}\|_2^2 + \lambda_1 \|\mathbf{Dx}\|_1 + \lambda_2 \|\mathbf{t}\|_* \quad s.t. \quad \mathbf{t} = \mathbf{x} \quad (6)$$

By applying augmented Lagrange, Eq.6 is turned into an unconstrained optimization problem:

$$\mathcal{L}(\mathbf{x}, \mathbf{t}, \boldsymbol{\alpha}) = \frac{1}{2} \|\mathbf{Ax} - \mathbf{y}\|_2^2 + \lambda_1 \|\mathbf{Dx}\|_1 + \lambda_2 \|\mathbf{t}\|_* - \langle \boldsymbol{\alpha}, \mathbf{t} - \mathbf{x} \rangle + \frac{\rho}{2} \|\mathbf{t} - \mathbf{x}\|_2^2 \quad (7)$$

where $\boldsymbol{\alpha}$ is a Lagrangian multiplier and ρ is a penalty parameter. A proximal point algorithm (PPA) [48] is applied to express the subproblems as

$$\begin{cases} \arg \min_{\mathbf{x}} \frac{1}{2} \|\mathbf{Ax} - \mathbf{y}\|_2^2 + \frac{\rho}{2} \|\mathbf{x} + \boldsymbol{\beta} - \mathbf{t}\|_2^2 + \lambda_1 \|\mathbf{Dx}\|_1 \\ \arg \min_{\mathbf{t}} \frac{\rho}{2} \|\mathbf{x} + \boldsymbol{\beta} - \mathbf{t}\|_2^2 + \lambda_2 \|\mathbf{t}\|_* \\ \boldsymbol{\beta} \leftarrow \boldsymbol{\beta} + \tilde{\eta}_1(\mathbf{x} - \mathbf{t}) \end{cases} \quad (8)$$

where $\boldsymbol{\beta} = \frac{\boldsymbol{\alpha}}{\rho}$ is a scaled Lagrangian multiplier and $\tilde{\eta}_1$ is an update rate. The subproblem of \mathbf{x} is a general l_1 norm CS reconstruction model. The iterative shrinkage-thresholding algorithm (ISTA) [47] is a popular first order proximal method, which is well suited for solving this subproblem. Specifically, ISTA solves the subproblem of \mathbf{x} by iterating between the following update steps:

$$\begin{cases} \mathbf{r}^n = \mathbf{x}^{n-1} - \tilde{\eta}_2(\mathbf{A}^T(\mathbf{Ax}^{n-1} - \mathbf{y}) + \rho(\mathbf{x}^{n-1} + \boldsymbol{\beta}^{n-1} - \mathbf{t}^{n-1})) \\ \mathbf{x}^n = \arg \min_{\mathbf{x}} \|\mathbf{x} - \mathbf{r}^n\|_2^2 + \lambda_1 \|\mathbf{Dx}\|_1 \end{cases} \quad (9)$$

where $\tilde{\eta}_2$ is an update rate. Substitute Eq.9 into Eq.8 and we

get the following formula:

$$\begin{cases} \mathbf{r}^n = \mathbf{x}^{n-1} - \tilde{\eta}_2(\mathbf{A}^T(\mathbf{Ax}^{n-1} - \mathbf{y}) + \rho(\mathbf{x}^{n-1} + \boldsymbol{\beta}^{n-1} - \mathbf{t}^{n-1})) \\ \mathbf{x}^n = \arg \min_{\mathbf{x}} \|\mathbf{x} - \mathbf{r}^n\|_2^2 + \lambda_1 \|\mathbf{Dx}\|_1 \\ \mathbf{t}^n = \arg \min_{\mathbf{t}} \frac{\rho}{2} \|\mathbf{x}^n + \boldsymbol{\beta}^{n-1} - \mathbf{t}\|_2^2 + \lambda_2 \|\mathbf{t}\|_* \\ \boldsymbol{\beta}^n = \boldsymbol{\beta}^{n-1} + \tilde{\eta}_1(\mathbf{x}^n - \mathbf{t}^n) \end{cases} \quad (10)$$

For the subproblem of \mathbf{x}^n , how to solve \mathbf{x}^n effectively and efficiently is critical. Optimization methods such as ADMM [49] and AMP [50] provide effective methods to solve \mathbf{x}^n . When the sparse transform \mathbf{D} is orthogonal (for example \mathbf{D} is wavelet transform), we can obtain \mathbf{x} by simple threshold operation: $\mathbf{x}^n = \mathbf{D}^T \text{soft}(\mathbf{Dr}^n, \lambda_1)$. However, it remains non-trivial to solve \mathbf{x}^n for a non-orthogonal transform \mathbf{D} . For simplicity of calculation, this paper focuses on the case where \mathbf{D} is orthogonal. For the subproblem of \mathbf{t}^n , an iterative singular value thresholding (IST) scheme [45] is used in the nuclear norm minimization and we obtain:

$$\mathbf{t}^n = \text{IST}(\mathbf{x}^n) = \sum_{i=0}^{\min(m,n)} (\Sigma_i - \lambda_2 \Sigma_i^{p-1} / \rho)_{+} \mathbf{u}_i \mathbf{v}_i^* \quad (11)$$

where $\mathbf{u}_i, \mathbf{v}_i$ and Σ_i are the singular vectors and values of \mathbf{x}^n . And the thresholding function $(\sigma)_+$ is defined as

$$(\sigma)_+ = \begin{cases} \sigma, & \text{if } \sigma \geq 0 \\ 0, & \text{else} \end{cases} \quad (12)$$

Finally, the sparse and low-rank MR model obtains the following iterative procedures:

$$\begin{cases} \mathbf{R}^n : \quad \mathbf{r}^n = \mathbf{x}^{n-1} - \tilde{\eta}_2(\mathbf{A}^T(\mathbf{Ax}^{n-1} - \mathbf{y}) + \rho(\mathbf{x}^{n-1} + \boldsymbol{\beta}^{n-1} - \mathbf{t}^{n-1})) \\ \mathbf{X}^n : \quad \mathbf{x}^n = \mathbf{D}^T \text{soft}(\mathbf{Dr}^n, \lambda_1) \\ \mathbf{T}^n : \quad \mathbf{t}^n = \text{IST}(\mathbf{x}^n) = \sum_{i=0}^{\min(m,n)} (\Sigma_i - \lambda_2 \Sigma_i^{p-1} / \rho)_{+} \mathbf{u}_i \mathbf{v}_i^* \\ \mathbf{M}^n : \quad \boldsymbol{\beta}^n = \boldsymbol{\beta}^{n-1} + \tilde{\eta}_1(\mathbf{x}^n - \mathbf{t}^n) \end{cases} \quad (13)$$

In traditional CS-MRI, an optimized reconstruction result \mathbf{x}^* can be obtained by iteratively solving Eq.13. However, both hyper-parameters $\{\lambda_1, \lambda_2, \rho, \tilde{\eta}_1, \tilde{\eta}_2\}$ and sparse transform \mathbf{D} need to be selected empirically, which is tedious and uncertain. What's worse, iterative solution often takes a long time, which limits its clinical application.

In this paper, a deep sparse and low-rank network has been proposed, dubbed as SLR-Net. It unrolls the SLR model of Eq.5 into a deep neural network. In this way, the SLR-Net can explore the sparse and low-rank prior of dynamic MR images simultaneously. Reconstruction performance will also be further improved by combining the multiple priors of dynamic MR images. To the best of our knowledge, this is the first time that a sparse and low-rank MR model has been unrolled into the network.

Specifically, our SLR-Net is defined over the iterative procedures of Eq.13. The four procedures in Eq.13 correspond to the four modules in SLR-Net as shown in Fig.1, which are named as reconstruction layer \mathbf{R}^n , sparse prior layer \mathbf{X}^n , low-rank prior layer \mathbf{T}^n and multiplier update layer \mathbf{M}^n respectively. SLR-Net keeps the same arithmetic structures, but

its hyper-parameters $\{\lambda_1, \lambda_2, \rho, \tilde{\eta}_1, \tilde{\eta}_2\}$ and sparse transform \mathbf{D} are learnable. We next discuss the four modules in details.

- **Reconstruction layer \mathbf{R}^n :** The reconstruction result of the current iteration or layer \mathbf{r}^n can be obtained under the given $\{\mathbf{x}^{n-1}, \boldsymbol{\beta}^{n-1}, \mathbf{t}^{n-1}\}$ according to Eq.13. The hyper-parameter ρ and $\tilde{\eta}_2$ are set as network learnable parameters, which initialized to zero and 0.1 respectively. When $n = 1$, \mathbf{x}^0 is the zero-filling image, and $\{\boldsymbol{\beta}^0, \mathbf{t}^0\}$ are initialized to zeros.
- **Sparse prior layer \mathbf{X}^n :** This layer explores the sparse prior of current reconstruction \mathbf{r}^n . \mathbf{x}^n can be obtained according to Eq.13. Unlike traditional CS-MRI, where the sparse transform \mathbf{D} is designed empirically, the SLR-Net can learn a general sparse transform \mathbf{D} using convolutional neural networks. And we don't strictly require \mathbf{D} and \mathbf{D}^T to be transpose to each other. Instead, they are learned by different networks $\{\tilde{\mathbf{D}}_1, \tilde{\mathbf{D}}_2\}$ to increase the network capacity. Three convolutional layers are used to learn the transforms.
- **Low-rank prior layer \mathbf{T}^n :** To solve the low-rank constrained subproblem, IST is used in nuclear norm minimization with soft threshold scheme. In this paper, we proposed a learnable low-rank prior for the first time:

$$\begin{cases} \mathbf{t}^n = \mathbf{U}H_k(\boldsymbol{\Sigma})\mathbf{V}^* \\ H_k(\boldsymbol{\Sigma}) = \text{diag}(\tilde{\boldsymbol{\sigma}}) \\ \tilde{\boldsymbol{\sigma}} = \begin{cases} \sigma_i, & \text{if } 1 \leq i \leq k \\ \omega_i \sigma_i, & \text{if } k < i \leq t \end{cases} \end{cases} \quad (14)$$

where $\mathbf{x}^n = \mathbf{U}\boldsymbol{\Sigma}\mathbf{V}^*$ is the singular value decomposition of \mathbf{x}^n . H_k is a learned singular value thresholding (SVT) operation. Specifically, the singular values of top k are completely retained, and the remaining singular values are weighted for suppression. The weights $\{\omega_i\}_{k < i \leq t}$ is learned through a multi-layer perceptron (MLP) network, and the sigmoid activation function is used to ensure that the weights are between 0 and 1. In addition, these weights are applied with coefficients of exponential decay as follow:

$$\omega_i = \exp^{-0.5i} \text{MLP}(\boldsymbol{\sigma})_i \quad (15)$$

The proposed MLP consists of two fully connected layers with 16 nodes.

- **Multiplier update layer \mathbf{M}^n :** This layer is used to update the Lagrange multiplier $\boldsymbol{\beta}$. $\tilde{\eta}_1$ is a learned parameter.

Our proposed deep SLR-Net has the following advantages: 1). The deep architecture can effectively combine the sparse and low-rank prior and further improve the reconstruction results. 2). All of the hyper-parameters and transforms can be learned by the proposed network, which eliminates the complex and lengthy selections of parameters and transforms. 3). Once the optimal network parameters are learned, the reconstructed image can be obtained by flowing the test data through the network diagram in seconds, which avoids the tedious iterations in traditional CS-MRI.

C. The Second Scheme: The Proposed Plug-and-play LR Network Module

In the first scheme, the low-rank prior of dynamic data has been introduced by unrolling a sparse and low-rank based optimization algorithm. However, the optimization algorithm is highly customized, and currently no simple turn-key deep learning methods exist to match low-rank as a prior for general inverse problems. Inspired by [51], we provide another scheme to explore the low-rank prior in a network via a plug-and-play LR network module for a general inverse problem. The plug-and-play LR network module can be easily embedded into other deep learning models without changing the network paradigm. This paper lists, but not limited to, three instances of how to embed the proposed learned LR module as shown in Fig.2. Fig.2 (a, b, c) represent the original ISTA-Net [52], DC-CNN [39] and CRNN [40] respectively and Fig.2 (d, e, f) represent their respective models embedded with the plug-and-play LR module, which dubbed as ISTA-LR-Net, DC-CNN-LR and CRNN-LR. ISTA-Net is an unrolled network developed by applying ISTA algorithm to solve the sparse optimization problem in Eq.1. Its iterative procedures is shown in the following formula:

$$\begin{cases} \mathbf{R}^n : \mathbf{r}^n = \mathbf{x}^{n-1} - \tilde{\eta}(\mathbf{A}^T(\mathbf{A}\mathbf{x}^{n-1} - \mathbf{y})) \\ \mathbf{X}^n : \mathbf{x}^n = \mathbf{D}^T \text{soft}(\mathbf{D}\mathbf{r}^n, \lambda) \end{cases} \quad (16)$$

The learned LR module \mathbf{T}^n performs SVT operations on the input signal as shown in Eq.14. There are three locations (L1, L2, L3) where the LR module can be embedded as shown in the dotted circle in Fig.2 (d, e, f). If the LR module is embedded before the CNN network, the low-rank prior are loaded into the dynamic signal, and the network will learn the sparse and low-rank features of the signal. If the LR module is embedded after the CNN network, the LR module is used for low-rank correction of predicted results to ensure its low-rank prior, just like the DC module for k-space correction of predicted results. The embedded LR module implies that the model favours the low-rank solution.

Although in this scheme, the LR module can be flexibly embedded at different locations in different networks, it does not mean that it is unwarranted. Next, we will take ISTA-LR-Net (L3) as an example to give its theoretical explanation.

The ISTA-LR-Net conforms to the following iterative procedures:

$$\begin{cases} \mathbf{R}^n : \mathbf{r}^n = \mathbf{x}^{n-1} - \tilde{\eta}(\mathbf{A}^T(\mathbf{A}\mathbf{x}^{n-1} - \mathbf{y})) \\ \mathbf{X}^n : \mathbf{x}^n = \mathbf{D}^T \text{soft}(\mathbf{D}\mathbf{r}^n, \lambda) \\ \mathbf{T}^n : \mathbf{t}^n = \mathbf{U}H_k(\boldsymbol{\Sigma})\mathbf{V}^* \end{cases} \quad (17)$$

The above formula can be derived from the following derivation. To solve problem (Eq.1), the iteration of ISTA can be

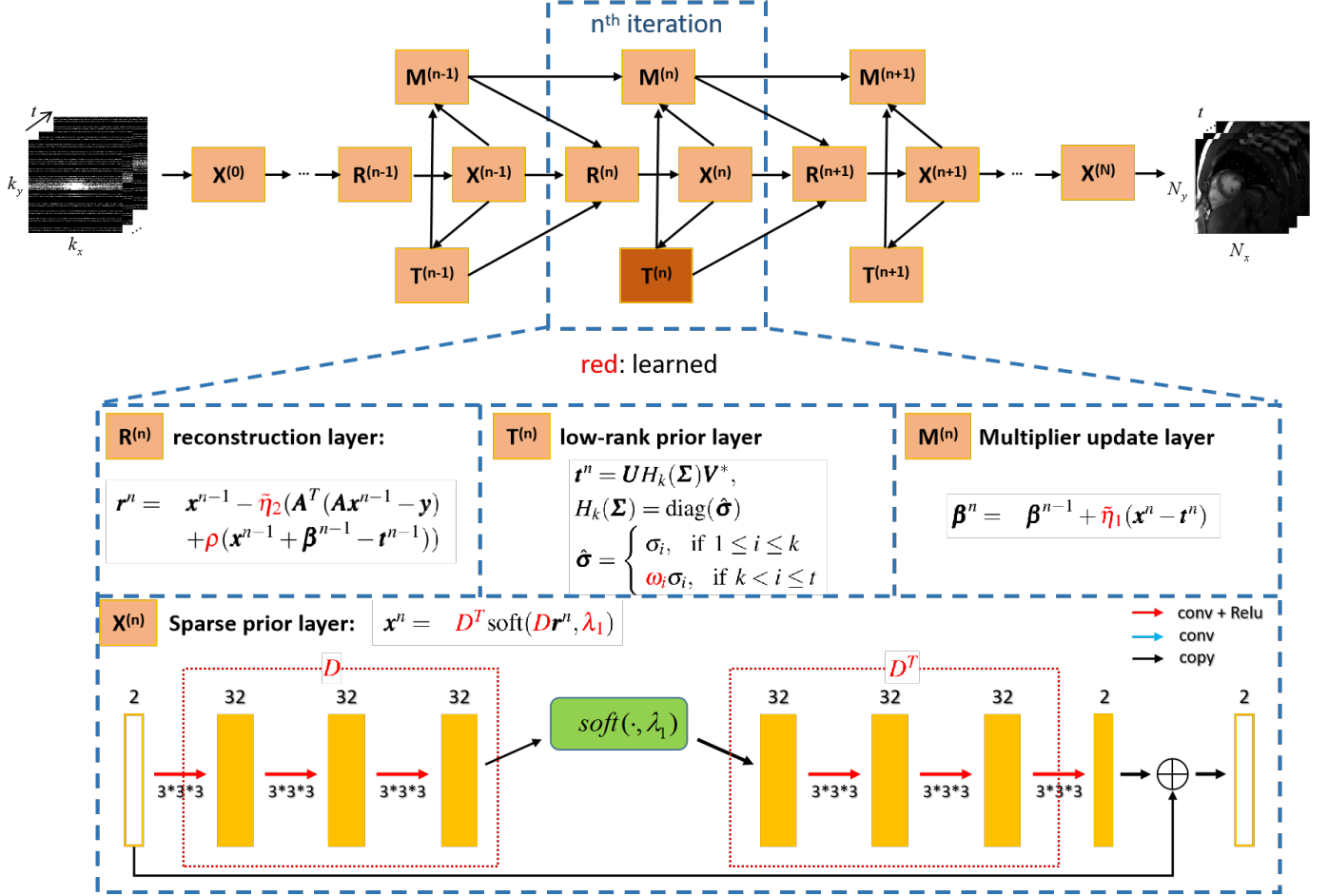


Fig. 1. The proposed sparse and low-rank network (SLR-Net) for dynamic MRI. The SLR-Net is defined over the iterative procedures of Eq.13. The four procedures in Eq.13 correspond to the four modules in SLR-Net, which are named as reconstruction layer \mathbf{R}^n , sparse prior layer \mathbf{X}^n , low-rank prior layer \mathbf{T}^n and multiplier update layer \mathbf{M}^n respectively. SLR-Net keeps the same arithmetic structures, but its hyper-parameters and sparse transform are learnable.

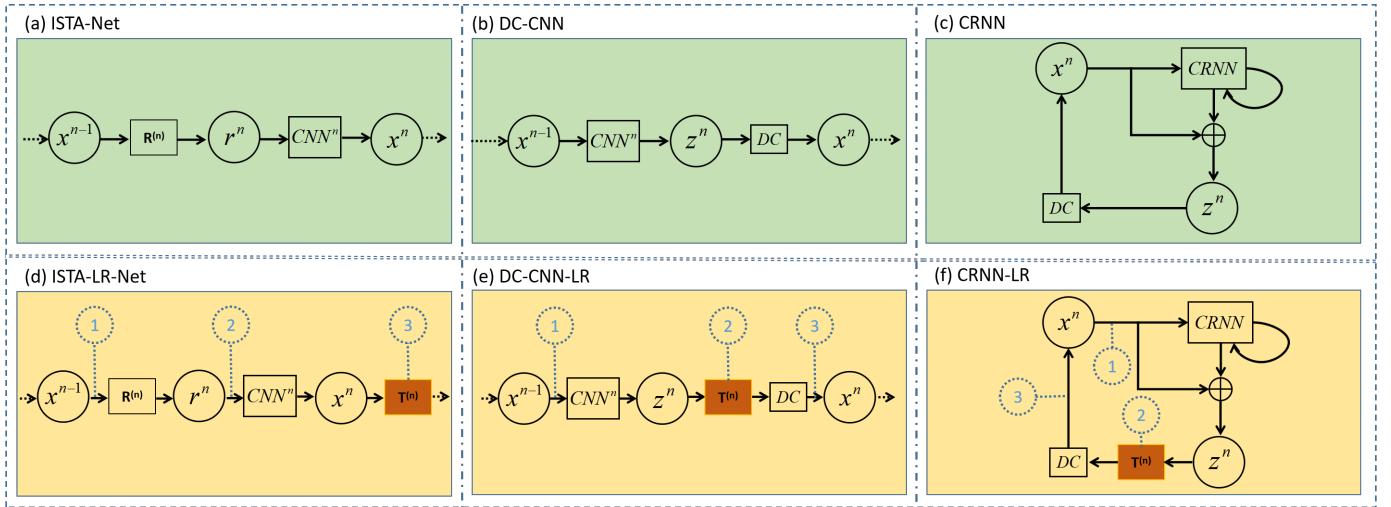


Fig. 2. The proposed plug-and-play LR network module. (a) The original ISTA-Net. (b) The original DC-CNN. (c) The original CRNN. (d) ISTA-LR-Net by embedding the LR network module into the original ISTA-Net. (e) DC-CNN-LR by embedding the LR network module into the original DC-CNN. (f) CRNN-LR by embedding the LR network module into the original CRNN. The numbers in the dotted box represent the locations where the LR module can be embedded.

formulated as

$$\begin{aligned} \mathbf{x}^n &= \arg \min_{\mathbf{x}} \langle \mathbf{A}^T(\mathbf{Ax}^{n-1} - \mathbf{y}), \mathbf{x} - \mathbf{x}^{n-1} \rangle + \frac{1}{2\tilde{\eta}} \|\mathbf{x} - \mathbf{x}^{n-1}\|^2 \\ &\quad + \lambda_1 \|\mathbf{Dx}\|_1 \\ &= \arg \min_{\mathbf{x}} \frac{1}{2\tilde{\eta}} \|\mathbf{x} - (\mathbf{x}^{n-1} - \tilde{\eta} \mathbf{A}^T(\mathbf{Ax}^{n-1} - \mathbf{y}))\|^2 \\ &\quad + \lambda_1 \|\mathbf{Dx}\|_1 \end{aligned} \quad (18)$$

which can be viewed as an inexact method that the first-order Taylor approximation is used for the data fidelity $\|\mathbf{Ax}^n - \mathbf{y}\|$ at each iteration. Here, we propose to promote the ISTA algorithm solve problem (Eq.5), where the combination of sparsity promoting regularizer $\lambda_1 \|\mathbf{Dx}\|_1$ and low rank regularizer $\lambda_2 \|\mathbf{x}\|_*$ is considered. With the same methodology, approximating the objective of (Eq.5) by first-order Taylor approximation for the data fidelity $\|\mathbf{Ax}^n - \mathbf{y}\|$ at \mathbf{x}^{n-1} and for the regularizer $\lambda_1 \|\mathbf{Dx}\|_1$ at \mathbf{x}^n , at the n -th iteration, we derive an approximated objective function as follows:

$$\begin{aligned} J(\mathbf{t}) &:= \langle \mathbf{A}^T(\mathbf{Ax}^{n-1} - \mathbf{y}), \mathbf{t} - \mathbf{x}^{n-1} \rangle + \langle \lambda_1 g^n, \mathbf{t} - \mathbf{x}^n \rangle \\ &\quad + \frac{1}{2\tilde{\eta}} \|\mathbf{r} - \mathbf{x}^{n-1}\|^2 + \lambda_2 \|\mathbf{x}\|_* \end{aligned} \quad (19)$$

where $g^n \in \partial \|\mathbf{Dx}^n\|$. Update the variable according to the rule of ISTA, i.e., $\mathbf{t}^n = \arg \min_{\mathbf{t}} J(\mathbf{t})$, we have

$$\begin{aligned} \mathbf{t}^n &= \arg \min_{\mathbf{t}} \frac{1}{2\tilde{\eta}} \|\mathbf{t} - (\mathbf{x}^{n-1} - \tilde{\eta} \mathbf{A}^T(\mathbf{Ax}^{n-1} - \mathbf{y}) - \tilde{\eta} \lambda_1 g^n)\|^2 \\ &\quad + \lambda_2 \|\mathbf{x}\|_* \end{aligned} \quad (20)$$

By the first-order optimization condition of (18), we have

$$\mathbf{x}^n = \mathbf{x}^{n-1} - \tilde{\eta} \mathbf{A}^T(\mathbf{Ax}^{n-1} - \mathbf{y}) - \tilde{\eta} \lambda_1 g^n. \quad (21)$$

Substituting (21) into (19), and by the definition of nuclear norm proximal operator, we have

$$\mathbf{t}^n = \mathbf{UH}_k(\boldsymbol{\Sigma})\mathbf{V}^T \quad (22)$$

On the other hand, directly from (18), (21) can be reformulated as following two steps:

$$\begin{aligned} \mathbf{r}^n &= \mathbf{x}^{n-1} - \tilde{\eta} \mathbf{A}^T(\mathbf{Ax}^{n-1} - \mathbf{y}) \\ \mathbf{x}^n &= \mathbf{D}^T \text{soft}(\mathbf{Dr}^n, \lambda_1 \tilde{\eta}) \end{aligned} \quad (23)$$

With (22) and (23) together, the formula (25) is derived.

III. EXPERIMENTAL RESULTS

A. Setup

1) *Data acquisition*: We collected 386 2D dynamic (2Dt) fully sampled cardiac MR data from 30 healthy volunteers using a 3T scanner (SIEMENS MAGNETOM Trio) with a balanced steady-state free precession (bSSFP) sequence. All the in vivo experiments were approved by the Institutional Review Board (IRB) of Shenzhen Institutes of Advanced Technology, and informed consent was obtained from each volunteer. Each scan contains a single-slice bSSFP acquisition with 25 temporal frames. Retrospectively electrocardiogram ECG-gated segmented imaging was conducted, and each slice was acquired in one breath-hold of 15-20 sec. The following parameters were used for the bSSFP scans: FOV 330×330

mm, acquisition matrix 256×256 , slice thickness = 6 mm, TR/TE = 3.0 ms/1.5 ms and 20 receiving coils. The temporal resolution is 40.0 ms. The raw multi-coil data of each frame was combined by adaptive coil combine method [53] to produce a single-channel complex-valued image. We focused on the single-channel scenario because the low-rank module occupies a huge GPU memory. It is difficult to explore low-rank prior and parallel image simultaneously under the current hardware conditions. We randomly selected 25 volunteers for training and the rest for testing. Deep learning typically require a large amount of data for training [54]. Therefore, some data augmentation strategies were applied. The data augmentation pattern that we chose was rigid transformation-shearing. We sheared the original multichannel images along the x, y and t directions. The sheared size was $192 \times 192 \times 16$ ($x \times y \times t$), and the stride along the three directions is 15, 15 and 1 respectively. Finally, we obtained 1548 2Dt cardiac MR data of size $192 \times 192 \times 16$ ($x \times y \times t$) for training and 45 data for testing.

Retrospective undersampling was performed to generate input/output pairs for network training. We focus on cartesian undersampling pattern because it is the most common protocol in the clinical. For each frame, the original k-space was retrospectively undersampled with 4 lowest spatial frequencies. Specifically, we fully sampled frequency-encodes (along k_x) and randomly undersampled the phase encodes (along k_y) according to a zero-mean Gaussian variable density function [8] as shown in Fig.3.

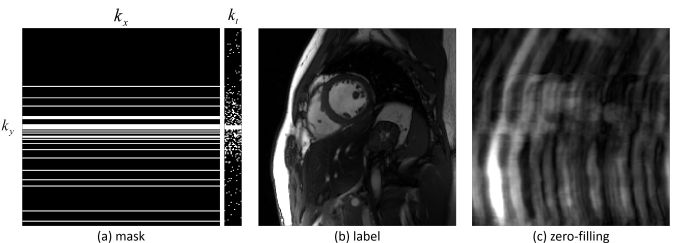


Fig. 3. The gaussian variable density undersampling mask used in this work at 8-fold. (a) mask. (b) label. (c) zero-filling image.

2) *Model configuration*: To demonstrate the effectiveness of the unrolling manner in dynamic MR imaging, we compared it with the state-of-the-art classical k-t SLR [17]. The k-t SLR method selected its single-channel versions. For fair comparisons, we adjusted the parameters of the k-t SLR method to its best performance. And to demonstrate the positive effects of the deep low-rank prior in SLR-Net, we set a control group, where λ_2 was set to 0, so that the deep low-rank prior does not play a role, dubbed as S-Net.

To demonstrate the effectiveness of the plug-and-play LR module, we embeded it in the state-of-the-art CNN-based DC-CNN [39] and CRNN [40] methods, as shown in Fig.2. They were executed according to the source code provided by the authors. For the DC-CNN method, we focused on a D5C5 model, which works pretty well for this method.

All the CNN-based methods keep the same hyperparameters. For network training, we divided each data into two channels, where the channels stored real and imaginary

parts of the data. So the inputs of the network are undersampled k-space $\mathbb{C}^{2N_x N_y N_t}$ and the outputs are reconstruction images $\mathbb{C}^{2N_x N_y N_t}$. SLR-Net has 8 iterative steps, that is, $N = 8$. The singular value in the low-rank layer and LR module takes top 8 for threshold operation, that is, $k = 8$. Each convolutional layer has 32 convolution kernels and the size of each convolution kernel is $3 \times 3 \times 3$. He initialization [55] was used to initialize the network weights. Rectifier Linear Units (ReLU) [56] were selected as the nonlinear activation functions. The mini-batch size was 4. The exponential decay learning rate [57] was used in all CNN-based experiments and the initial learning rate was set to 0.001 with a decay of 0.95. All the models were trained by the Adam optimizer [58] with parameters $\beta_1 = 0.9$, $\beta_2 = 0.999$ and $\epsilon = 10^{-8}$.

The models were implemented on an Ubuntu 16.04 LTS (64-bit) operating system equipped with an Intel Xeon Gold 5120 Processor Central Processing Unit (CPU) and Tesla V100 Graphics Processing Unit (GPU, 32GB memory) in the open framework Tensorflow [59] with CUDA and CUDNN support. The network training took approximately 18 hours within 50 epochs.

3) *Performance evaluation*: For a quantitative evaluation, mean square error (MSE), peak signal to noise ratio (PSNR) and structural similarity index (SSIM) [60] were measured as follows:

$$\text{MSE} = \|\text{Ref} - \text{Rec}\|_2^2 \quad (24)$$

$$\text{PSNR} = 20 \log_{10} \frac{\max(\text{Ref}) \sqrt{N}}{\|\text{Ref} - \text{Rec}\|_2} \quad (25)$$

$$\text{SSIM} = \mathbf{l}(\text{Ref}, \text{Rec}) \cdot \mathbf{c}(\text{Ref}, \text{Rec}) \cdot \mathbf{s}(\text{Ref}, \text{Rec}) \quad (26)$$

where Rec is the reconstructed image, Ref denotes the reference image and N is the total number of image pixels. The SSIM index is a multiplicative combination of the luminance term, the contrast term, and the structural term (details shown in [60]).

B. The Reconstruction Performance of the Proposed SLR-Net

To demonstrate the efficacy of the proposed deep unrolling method, we compared it with a state-of-the-art CS-LR method k-t SLR [17]. We adjusted the parameters of the competing method to its best performance. The reconstruction results of these methods at 8-fold acceleration are shown in Fig.4. We present both diastolic and systolic reconstruction results to demonstrate the good performance of our proposed SLR-Net for different heart phases. The left half shows diastolic reconstruction results, and the right half shows systolic reconstruction results. The first row shows, from left to right, the ground truth, the reconstruction result of these methods. The second row shows the enlarged view of their respective heart regions framed by a yellow box. The third row shows the error map (display ranges [0, 0.07]). The y-t image (extraction of the 124th slice along the y and temporal dimensions) and the error of y-t image are also given for each signal to show the reconstruction performance in the temporal dimension. The reconstruction performance of the two deep learning based methods (ISTA-Net and SLR-Net) is better than that of the traditional iterative method (k-t SLR), which can be clearly

TABLE I
THE AVERAGE MSE, PSNR, SSIM AND RECONSTRUCTION TIME OF K-T SLR, ISTA-NET AND SLR-NET ON THE TEST DATASET AT 8-FOLD ACCELERATION (MEAN \pm STD).

Methods	MSE(*e-5)	PSNR	SSIM	Time(s)
k-t SLR	9.49 ± 3.05	40.65 ± 1.99	0.9502 ± 0.0067	197.49
ISTA-Net	5.64 ± 1.65	42.68 ± 1.33	0.9710 ± 0.0057	0.23
SLR-Net	3.82 ± 1.31	44.43 ± 1.55	0.9787 ± 0.0054	0.66

seen from the error maps. The comparison between the two deep learning methods shows that SLR-Net is better than ISTA-Net in both detail retention and artifact removal (as shown by the green and red arrows). This indicates that the deep low-rank prior plays an important role in dynamic MR reconstruction. The y-t results also have consistent conclusions, as shown by the yellow arrows. We also provided the quantitative evaluations in Table I. One can see that the SLR-Net achieves optimal quantitative evaluations. Although the introduction of deep low-rank increases the amount of computation, the effect on the reconstruction time is very small and can even be ignored compared with the reconstruction time of k-t SLR. In both qualitative and quantitative results, we can draw a conclusion: the proposed first deep low-rank prior scheme, an unrolling sparse and low-rank network, can effectively explore the low-rank prior of dynamic data, thus improving the reconstruction performance.

C. The Reconstruction Performance of the Proposed Plug-and-play LR Module

To demonstrate the efficacy of the proposed plug-and-play LR module, we embed it in the state-of-the-art CNN-based DC-CNN [39] and CRNN [40] methods at location numbered 2 (L2), as shown in Fig.2.

The reconstruction results of CNN-LR at 8-fold acceleration are shown in Fig.5. It is obvious to observe that by embedding LR module, the reconstruction results have more details (as shown in the green arrow) and the smoothness is eliminated. The quantitative evaluations were also provided in Table II. All three performance metrics were significantly improved (DC-CNN: 1.5e-5 lower in MSE, 1.1dB higher in PSNR and 0.006 higher in SSIM. CRNN: 1.9e-5 lower in MSE, 1.4dB higher in PSNR and 0.008 higher in SSIM). Both qualitatively and quantitatively, our second deep low-rank prior scheme has achieved great success.

DC-CNN and CRNN have consistent conclusions: The embedding of LR module can effectively improve the reconstruction results. This lightweight LR module enables the neural networks to quickly access low-rank prior of dynamic data. It is also very easy to embed in other dynamically correlated deep learning models because it does not require changes to the topology of the network.

IV. DISCUSSION

A. The Locations Where the LR Module is Embedded

In the second scheme, the LR Module can be embedded into any other dynamic deep networks. However, whether the LR

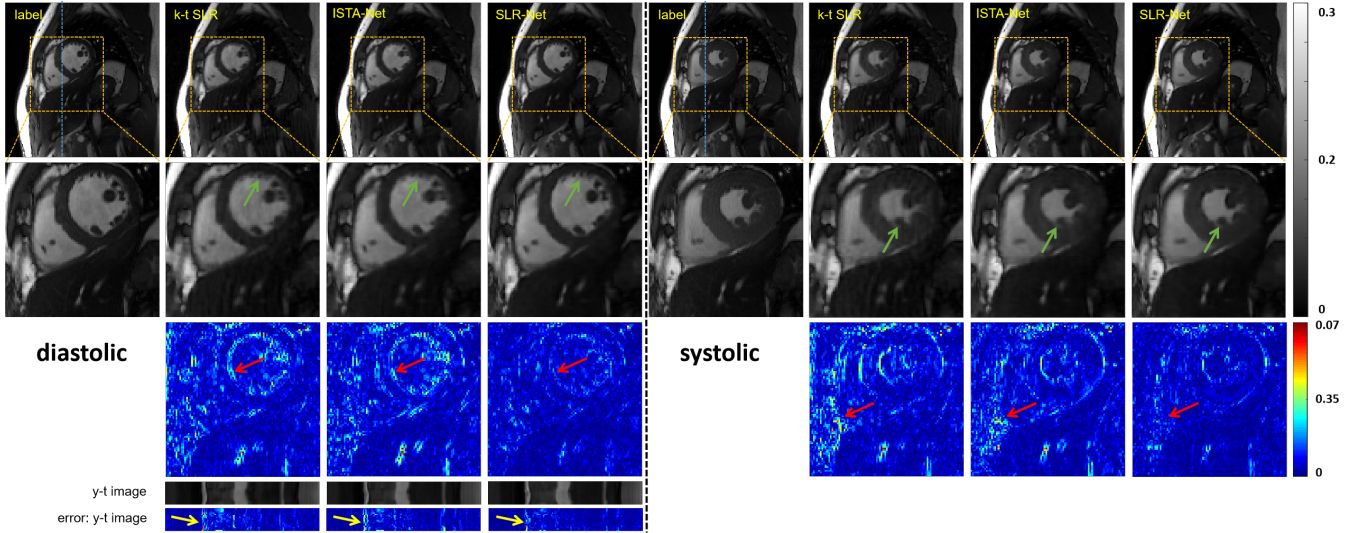


Fig. 4. The reconstruction results of the different methods (k-t SLR, ISTA-Net and the proposed SLR-Net) at 8-fold acceleration. The left half shows diastolic reconstruction, and the right half shows systolic reconstruction. The first row shows, from left to right, the ground truth, the reconstruction result of these methods. The second row shows the enlarged view of their respective heart regions framed by a yellow box. The third row shows the error map (display ranges [0, 0.07]). The y-t image (extraction of the 124th slice along the y and temporal dimensions) and the error of y-t image are also given for each signal to show the reconstruction performance in the temporal dimension.

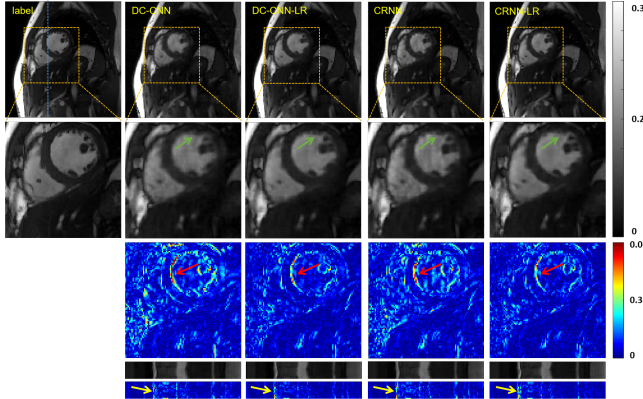


Fig. 5. The reconstruction results of the different methods (DC-CNN, DC-CNN-LR, CRNN and CRNN-LR) at 8-fold acceleration. The first row shows, from left to right, the ground truth, the reconstruction result of these methods. The second row shows the enlarged view of their respective heart regions framed by a yellow box. The third row shows the error map (display ranges [0, 0.07]). The y-t image (extraction of the 124th slice along the y and temporal dimensions) and the error of y-t image are also given for each signal to show the reconstruction performance in the temporal dimension.

TABLE II
THE AVERAGE MSE, PSNR AND SSIM OF DC-CNN/DC-CNN-LR AND CRNN/CRNN-LR ON THE TEST DATASET AT 8-FOLD ACCELERATION (MEAN \pm STD).

Methods	MSE(*e-5)	PSNR	SSIM
DC-CNN	7.49 \pm 2.24	41.46 \pm 1.36	0.9644 \pm 0.0070
DC-CNN-LR	5.93 \pm 1.93	42.52 \pm 1.48	0.9702 \pm 0.0065
CRNN	7.18 \pm 2.12	41.63 \pm 1.34	0.9668 \pm 0.0063
CRNN-LR	5.27 \pm 1.76	43.04 \pm 1.53	0.9741 \pm 0.0061

module is embedded anywhere works, or where it is embedded to achieve the best reconstruction performance is still un-

known. In this section, without loss of generality, we take DC-CNN as an example to explore the reconstruction performance when LR module is embedded in different locations (L1, L2 and L3 as shown in Fig. 2). Three DC-CNN-LR models were trained under exactly the same conditions. The only difference between them lay in the different embedding locations of LR modules. As can be seen from the reconstruction results in Fig. 6, no matter where LR is embedded, improved results can be achieved. This fully demonstrates the effectiveness and universality of the proposed plug-and-play LR module. The three DC-CNN-LR models achieved very similar reconstruction results, but the L2 model performed better in minimal detail, as shown by the green arrows. The quantitative evaluations are provided in Table III. The quantitative indicators of the three LR models are all consistently superior to the original DC-CNN model. The internal comparison of the three LR models shows that their quantitative indicators are very similar. The L2 model achieves the best quantization performance with a slight advantage. The quantization performance of L3 model is slightly weak, which may be because LR module is embedded behind DC module, which slightly damages the performance of DC module.

Based on the above results, we give the following suggestions for embedding LR modules: No matter where LR module is embedded in the network, one can improve the reconstruction performance, but try not to embed it behind DC module to avoid sacrificing the role of DC module.

B. Which of the Two Schemes Performs Better

The above sections demonstrate that both schemes that introduce deep low-rank prior can lead to improvements in the reconstructed results. In this section, we will explore which of these two schemes works better. To be fair, a same baseline is needed, and we regarded ISTA-Net as the baseline method.

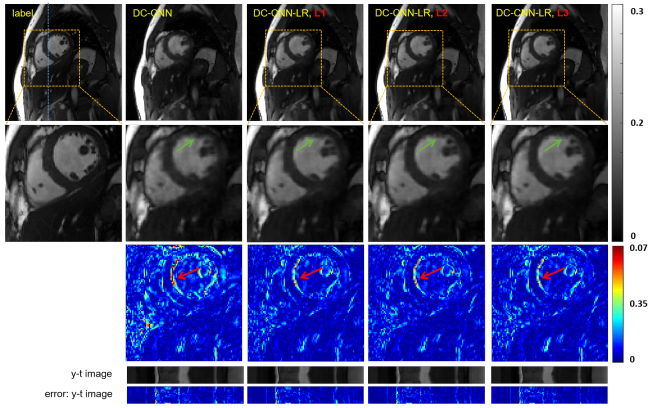


Fig. 6. The reconstruction results of DC-CNN-LR with different embedding locations of LR modules at 8-fold acceleration. The first row shows, from left to right, the ground truth, the reconstruction results of DC-CNN and DC-CNN-LR with three different locations. The second row shows the enlarged view of their respective heart regions framed by a yellow box. The third row shows the error map (display ranges [0, 0.07]). The y-t image (extraction of the 124th slice along the y and temporal dimensions) and the error of y-t image are also given for each signal to show the reconstruction performance in the temporal dimension.

TABLE III

THE AVERAGE MSE, PSNR AND SSIM OF DC-CNN AND DC-CNN-LR (L1, L2, L3) ON THE TEST DATASET AT 8-FOLD ACCELERATION (MEAN \pm STD).

Methods	MSE(*e-5)	PSNR	SSIM
DC-CNN	7.49 \pm 2.24	41.46 \pm 1.36	0.9644 \pm 0.0070
DC-CNN-LR, L1	6.00 \pm 1.89	42.44 \pm 1.42	0.9700 \pm 0.0063
DC-CNN-LR, L2	5.93 \pm 1.93	42.52 \pm 1.48	0.9702 \pm 0.0065
DC-CNN-LR, L3	6.35 \pm 2.02	42.20 \pm 1.44	0.9678 \pm 0.0068

Obviously, SLR-Net is the unrolling version of deep low-rank prior based on ISTA-Net. Its plug-and-play version of deep low-rank prior is ISTA-LR-Net as shown in Fig.2 (d). By comparing these two models, one can intuitively see which scheme performs better. The reconstruction results of these two models at 8-fold acceleration are shown in Fig.7. Both models have achieved better reconstruction performance, but SLR-Net has some advantages in preserving detail, as shown by the green arrow. SLR-Net also has certain progress in quantitative indicators, as shown in Table IV. Therefore, we come to the conclusion that under the same baseline, unrolled deep low-rank prior is superior to plug-and-play deep low-rank prior. The reason may be that unrolled deep low-rank prior is introduced according to mathematical derivation, which is more reasonable.

Both schemes have their own advantages and applicable scenarios: The mathematical interpretation of unrolled deep low-rank prior is stronger, and the reconstruction results are better. So the first scheme is recommended if one is looking for the best performance. The highlight of plug-and-play deep Low-rank prior is its portability. If a network model has been proved to be suitable for a particular application, it is non-trivial to build an unrolled network. Then, plug-and-play deep low-rank prior is recommended.

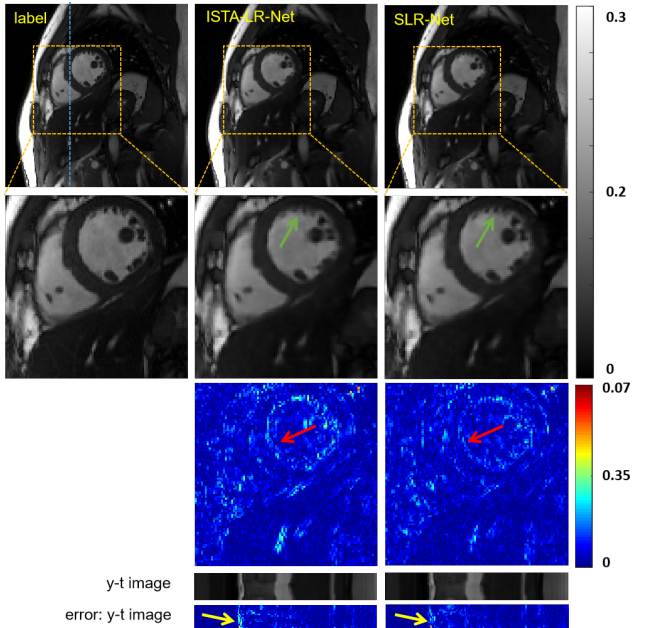


Fig. 7. The reconstruction results of ISTA-LR-Net and SLR-Net at 8-fold acceleration. The first row shows, from left to right, the ground truth, the reconstruction result of these methods. The second row shows the enlarged view of their respective heart regions framed by a yellow box. The third row shows the error map (display ranges [0, 0.07]). The y-t image (extraction of the 124th slice along the y and temporal dimensions) and the error of y-t image are also given for each signal to show the reconstruction performance in the temporal dimension.

TABLE IV
THE AVERAGE MSE, PSNR AND SSIM OF ISTA-LR-NET AND SLR-NET ON THE TEST DATASET AT 8-FOLD ACCELERATION (MEAN \pm STD).

Methods	MSE(*e-5)	PSNR	SSIM
ISTA-LR-Net	4.16 \pm 1.54	44.13 \pm 1.69	0.9773 \pm 0.0062
SLR-Net	3.82 \pm 1.31	44.43 \pm 1.55	0.9787 \pm 0.0054

C. Higher Acceleration: 10-fold and 12-fold

The proposed deep low rank prior methods can make use of both sparse and low rank prior of dynamic MR data, which not only improves the reconstruction performance, but also is expected to higher acceleration because more regularization terms are introduced into the optimization problem. Without loss of generality, we explore the reconstruction performance at higher accelerations on the proposed SLR-Net. The 10-fold and 12-fold accelerated reconstruction results can be found in Fig. 8. Our proposed SLR-Net still achieves superior reconstruction performance, whether it is 10-fold or 12-fold. At 10-fold acceleration, the proposed SLR-Net can achieve satisfactory reconstruction results. The anatomical details of the heart tissue can be easily found, and the blurring is not serious. At 12-fold acceleration, the proposed SLR-Net can still achieve acceptable reconstruction results, although it is a little vague, but most of the details are well preserved. The quantitative indicators are provided in Table V, from which we can see that our proposed SLR-Net still achieves a good quantitative performance at higher accelerations. Although we did not show the results of higher accelerations under the plug-

TABLE V
THE AVERAGE MSE, PSNR AND SSIM OF SLR-NET AT 10-FOLD AND 12-FOLD ACCELERATION ON THE TEST DATASET (MEAN \pm STD).

Methods	MSE(*e-5)	PSNR	SSIM
10x	k-t SLR	11.13 \pm 3.86	39.73 \pm 1.59
	ISTA-Net	6.98 \pm 2.11	41.77 \pm 1.38
	SLR-Net	5.57\pm1.41	42.79\pm1.41
12x	k-t SLR	25.69 \pm 8.62	36.19 \pm 1.69
	S-Net	9.92 \pm 2.40	40.21 \pm 1.41
	SLR-Net	9.14\pm2.68	40.59\pm1.34
0.9550\pm0.0080			

and-play scheme, we believe that similar conclusions can be drawn in this scheme.

D. The limitations of the Proposed Deep Low-rank Prior

Although the two proposed deep low-rank prior methods achieve improved reconstruction results, they still have the following limitations: 1) The low-rank module will greatly occupy GPU memory, which puts forward higher requirements for hardware. 2) This work focused on single-channel dynamic MR imaging. However, the spatial variance coil sensitivity provided by the phase array coil also plays an important role in fast MRI. It is difficult to explore low-rank prior and parallel image simultaneously under the current hardware conditions. 3) In the proposed LR module, we selected top k ($k=8$) singular values in the singular vector. However, there are many other SVT strategies can be chosen, even SVT can be learned. Unfortunately, we did not explore which SVT strategy is optimal. In future work, these limitations will be addressed.

V. CONCLUSION AND OUTLOOK

In this paper, we explore deep low-rank prior in dynamic MR imaging to obtain improved reconstruction results. In particular, we propose a learned low-rank prior with two novel and distinct schemes to introduce it into deep network architectures in an unrolling manner and a plug-and-play manner respectively. In the unrolling manner, we propose a model-based unrolling sparse and low-rank network for dynamic MR imaging, dubbed SLR-Net. The SLR-Net is defined over a deep network flow graphs, which is unrolled from the iterative procedures in Iterative Shrinkage-Thresholding Algorithm (ISTA) for optimizing a sparse and low-rank based dynamic MRI model. In the plug-and-play manner, we propose a plug-and-play LR network module that can be easily embedded into any other dynamic MR neural networks without changing the neural network paradigm. Experimental results show that both of the two schemes can improve the reconstruction results, no matter qualitatively and quantitatively. To the best of our knowledge, this is the first time that a deep low-rank prior has been applied in dynamic MR imaging.

ACKNOWLEDGMENT

This research was partly supported by the National Natural Science Foundation of China (61771463, 81830056,

U1805261, 81971611, 61871373, 81729003, 81901736); National Key R&D Program of China (2017YFC0108802 and 2017YFC0112903); Natural Science Foundation of Guangdong Province (2018A0303130132); Shenzhen Key Laboratory of Ultrasound Imaging and Therapy (ZDSYS20180206180631473); Shenzhen Peacock Plan Team Program (KQTD20180413181834876); Innovation and Technology Commission of the government of Hong Kong SAR (MRP/001/18X); Strategic Priority Research Program of Chinese Academy of Sciences (XDB25000000).

REFERENCES

- [1] Z. P. Liang, H. Jiang, C. P. Hess, and P. C. Lauterbur, “Dynamic imaging by model estimation,” in *IEEE Embs International Summer School on Biomedical Imaging*, 2003.
- [2] B. Madore, “Using UNFOLD to remove artifacts in parallel imaging and in partial-Fourier imaging,” *Magnetic Resonance in Medicine*, vol. 48, no. 3, pp. 493–501, 2002.
- [3] J. Tsao, P. Boesiger, and K. P. Pruessmann, “k-t BLAST and k-t SENSE: Dynamic MRI with high frame rate exploiting spatiotemporal correlations,” *Magnetic Resonance in Medicine*, vol. 50, 2003.
- [4] R. Otazo, D. Kim, L. Axel, and D. K. Sodickson, “Combination of compressed sensing and parallel imaging for highly accelerated first-pass cardiac perfusion MRI,” *Magnetic Resonance in Medicine*, vol. 64, no. 3, pp. p.767–776, 2010.
- [5] D. L. Donoho, “Compressed sensing,” *IEEE Transactions on Information Theory*, vol. 52, no. 4, pp. 1289–1306, 2006.
- [6] M. Lustig, D. L. Donoho, and J. M. Pauly, “Sparse MRI: The application of compressed sensing for rapid MR imaging,” *Magnetic Resonance in Medicine*, vol. 58, no. 6, pp. 1182–1195, 2007.
- [7] M. Lustig, J. M. Santos, D. L. Donoho, and J. M. Pauly, “k-t SPARSE: high frame rate dynamic mri exploiting spatio-temporal sparsity,” in *Proceedings of the 13th annual meeting of ISMRM, Paris*, no. 2420, 2006.
- [8] H. Jung, J. C. Ye, and E. Y. Kim, “Improved k-t BLAST and k-t SENSE using FOCUSS,” *Physics in Medicine & Biology*, vol. 52, no. 11, p. 3201, 2007.
- [9] D. Liang, E. V. DiBella, R.-R. Chen, and L. Ying, “k-t ISD: dynamic cardiac MR imaging using compressed sensing with iterative support detection,” *Magnetic resonance in medicine*, vol. 68, no. 1, pp. 41–53, 2012.
- [10] J. Caballero, A. N. Price, D. Rueckert, and J. V. Hajnal, “Dictionary learning and time sparsity for dynamic MR data reconstruction,” *IEEE Transactions on Medical Imaging*, vol. 33, no. 4, pp. 979–994, 2014.
- [11] Y. Wang and L. Ying, “Compressed sensing dynamic cardiac cine MRI using learned spatiotemporal dictionary,” *IEEE transactions on Biomedical Engineering*, vol. 61, no. 4, pp. 1109–1120, 2013.
- [12] U. Nakarmi, Y. Wang, J. Lyu, D. Liang, and L. Ying, “A kernel-based low-rank (KLR) model for low-dimensional

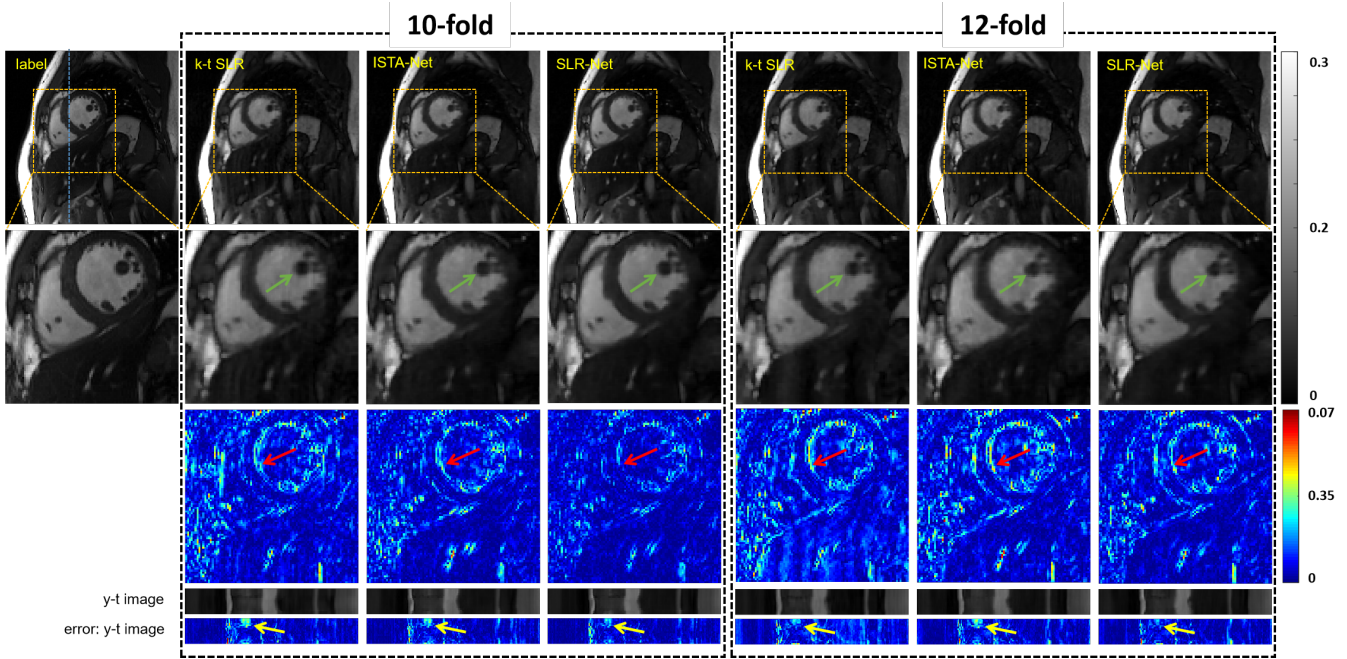


Fig. 8. The reconstruction results of the proposed SLR-Net at 10-fold and 12-fold acceleration. The left half shows 10-fold reconstruction, and the right half shows 12-fold reconstruction. The first row shows, from left to right, the ground truth, the reconstruction result of these methods. The second row shows the enlarged view of their respective heart regions framed by a yellow box. The third row shows the error map (display ranges [0, 0.07]). The y-t image (extraction of the 124th slice along the y and temporal dimensions) and the error of y-t image are also given for each signal to show the reconstruction performance in the temporal dimension.

manifold recovery in highly accelerated dynamic MRI,” *IEEE Transactions on Medical Imaging*, vol. PP, no. 99, pp. 1–1, 2017.

[13] G. N. Shetty, K. Slavakis, A. Bose, U. Nakarmi, G. Scutari, and L. Ying, “Bi-linear modeling of data manifolds for dynamic-MRI recovery,” *IEEE Transactions on Medical Imaging*, vol. 39, no. 3, pp. 688–702, 2019.

[14] Z. P. Liang, “Spatiotemporal imaging with partially separable functions,” in *2007 IEEE 4th International Symposium on Biomedical Imaging (ISBI)*, 2007, pp. 988–991.

[15] J. P. Haldar and Z.-P. Liang, “Spatiotemporal imaging with partially separable functions: A matrix recovery approach,” in *2010 IEEE International Symposium on Biomedical Imaging: From Nano to Macro*, 2010, pp. 716–719.

[16] B. Zhao, J. P. Haldar, A. G. Christodoulou, and Z.-P. Liang, “Image reconstruction from highly undersampled (k, t)-space data with joint partial separability and sparsity constraints,” *IEEE transactions on medical imaging*, vol. 31, no. 9, pp. 1809–1820, 2012.

[17] S. G. Lingala, Y. Hu, E. DiBella, and M. Jacob, “Accelerated dynamic MRI exploiting sparsity and low-rank structure: kt SLR,” *IEEE transactions on medical imaging*, vol. 30, no. 5, pp. 1042–1054, 2011.

[18] R. Otazo, E. Candes, and D. K. Sodickson, “Low-rank plus sparse matrix decomposition for accelerated dynamic MRI with separation of background and dynamic components,” *Magnetic Resonance in Medicine*, vol. 73, no. 3, pp. 1125–1136, 2015.

[19] J. Sun, H. Li, Z. Xu *et al.*, “Deep ADMM-Net for compressive sensing MRI,” in *Advances in neural information processing systems*, 2016, pp. 10–18.

[20] K. Hammernik, T. Klatzer, E. Kobler, M. P. Recht, D. K. Sodickson, T. Pock, and F. Knoll, “Learning a variational network for reconstruction of accelerated MRI data,” *Magnetic resonance in medicine*, vol. 79, no. 6, pp. 3055–3071, 2018.

[21] H. K. Aggarwal, M. P. Mani, and M. Jacob, “MoDL: Model-based deep learning architecture for inverse problems,” *IEEE transactions on medical imaging*, vol. 38, no. 2, pp. 394–405, 2018.

[22] T. Eo, Y. Jun, T. Kim, J. Jang, H.-J. Lee, and D. Hwang, “KIKI-net: cross-domain convolutional neural networks for reconstructing undersampled magnetic resonance images,” *Magnetic resonance in medicine*, vol. 80, no. 5, pp. 2188–2201, 2018.

[23] M. Akakaya, S. Moeller, S. Weingrtner, and K. Uurbil, “Scanspecific robust artificialneuralnetworks for kspace interpolation (RAKI) reconstruction: Databasefree deep learning for fast imaging,” *Magnetic Resonance in Medicine*, vol. 81, no. 1, pp. 439–453, 2018.

[24] J. Cheng, H. Wang, L. Ying, and D. Liang, “Model learning: Primal dual networks for fast MR imaging,” in *International Conference on Medical Image Computing and Computer-Assisted Intervention*. Springer, 2019, pp. 21–29.

[25] Y. Liu, Q. Liu, M. Zhang, Q. Yang, S. Wang, and D. Liang, “IFR-Net: Iterative feature refinement network for compressed sensing MRI,” *IEEE Transactions on*

Computational Imaging, vol. 6, pp. 434–446, 2019.

[26] H. Wang, J. Cheng, S. Jia, Z. Qiu, C. Shi, L. Zou, S. Su, Y. Chang, Y. Zhu, L. Ying *et al.*, “Accelerating MR imaging via deep chambolle-pock network,” in *2019 41st Annual International Conference of the IEEE Engineering in Medicine and Biology Society (EMBC)*. IEEE, 2019, pp. 6818–6821.

[27] S. Wang, Z. Su, L. Ying, X. Peng, S. Zhu, F. Liang, D. Feng, and D. Liang, “Accelerating magnetic resonance imaging via deep learning,” in *2016 IEEE 13th International Symposium on Biomedical Imaging (ISBI)*. IEEE, 2016, pp. 514–517.

[28] K. Kwon, D. Kim, and H. Park, “A parallel MR imaging method using multilayer perceptron,” *Medical physics*, vol. 44, no. 12, pp. 6209–6224, 2017.

[29] Y. Han, J. Yoo, H. H. Kim, H. J. Shin, K. Sung, and J. C. Ye, “Deep learning with domain adaptation for accelerated projection-reconstruction MR,” *Magnetic resonance in medicine*, vol. 80, no. 3, pp. 1189–1205, 2018.

[30] Y. Han, L. Sunwoo, and J. C. Ye, “ k -space deep learning for accelerated MRI,” *IEEE Transactions on Medical Imaging*, vol. 39, no. 2, pp. 377–386, 2020.

[31] B. Zhu, J. Z. Liu, S. F. Cauley, B. R. Rosen, and M. S. Rosen, “Image reconstruction by domain-transform manifold learning,” *Nature*, vol. 555, no. 7697, p. 487, 2018.

[32] L. Sun, Z. Fan, Y. Huang, X. Ding, and J. Paisley, “Compressed sensing MRI using a recursive dilated network,” in *Thirty-Second AAAI Conference on Artificial Intelligence*, 2018.

[33] T. M. Quan, T. Nguyen-Duc, and W.-K. Jeong, “Compressed sensing MRI reconstruction using a generative adversarial network with a cyclic loss,” *IEEE transactions on medical imaging*, vol. 37, no. 6, pp. 1488–1497, 2018.

[34] S. Wang, H. Cheng, L. Ying, T. Xiao, Z. Ke, X. Liu, H. Zheng, and D. Liang, “Deepcomplexmri: Exploiting deep residual network for fast parallel MR imaging with complex convolution,” *Magnetic Resonance Imaging*, vol. 68, pp. 136–147, 2019.

[35] D. Lee, J. Yoo, S. Tak, and J. Ye, “Deep residual learning for accelerated MRI using magnitude and phase networks,” *IEEE Transactions on Biomedical Engineering*, vol. 65, no. 9, pp. 1985–1995, 2018.

[36] L. Sun, Z. Fan, Y. Huang, X. Ding, and J. Paisley, “A deep information sharing network for multi-contrast compressed sensing MRI reconstruction,” *IEEE Transactions on Image Processing*, vol. 28, no. 12, pp. 6141–6153, 2018.

[37] Q. Liu, Q. Yang, H. Cheng, S. Wang, M. Zhang, and D. Liang, “Highly undersampled magnetic resonance imaging reconstruction using autoencoding priors,” *Magnetic resonance in medicine*, vol. 83, no. 1, pp. 322–336, 2020.

[38] D. Liang, J. Cheng, Z. Ke, and L. Ying, “Deep magnetic resonance image reconstruction: Inverse problems meet neural networks,” *IEEE Signal Processing Magazine*, vol. 37, no. 1, pp. 141–151, 2020.

[39] J. Schlemper, J. Caballero, J. V. Hajnal, A. N. Price, and D. Rueckert, “A deep cascade of convolutional neural networks for dynamic MR image reconstruction,” *IEEE Transactions on Medical Imaging*, vol. 37, no. 2, pp. 491–503, 2018.

[40] C. Qin, J. V. Hajnal, D. Rueckert, J. Schlemper, J. Caballero, and A. N. Price, “Convolutional recurrent neural networks for dynamic MR image reconstruction,” *IEEE Transactions on Medical Imaging*, vol. 38, no. 1, pp. 280–290, 2019.

[41] S. Wang, Z. Ke, H. Cheng, S. Jia, L. Ying, H. Zheng, and D. Liang, “DIMENSION: Dynamic MR imaging with both k -space and spatial prior knowledge obtained via multi-supervised network training,” *NMR in Biomedicine*, vol. e4131, 2019.

[42] C. Brinegar, Y. J. Wu, L. Fley, K. Hitchens, Q. Ye, C. Ho, and Z. P. Liang, “Real-time cardiac mri without triggering, gating, or breath holding,” in *30th Annual International Conference of the IEEE Engineering in Medicine and Biology Society*, 2008, pp. 3381–3384.

[43] H. Pedersen, S. Kozerke, S. Ringgaard, K. Nehrke, and W. Y. Kim, “ kt PCA: Temporally constrained kt BLAST reconstruction using principal component analysis,” *Magnetic Resonance in Medicine*, vol. 62, no. 3, 2009.

[44] E. J. Cands and B. Recht, “Exact matrix completion via convex optimization,” *Foundations of Computational Mathematics*, vol. 9, no. 6, p. 717, 2008.

[45] J. F. Cai, E. J. Cands, and Z. Shen, “A singular value thresholding algorithm for matrix completion,” *Siam Journal on Optimization*, vol. 20, no. 4, pp. 1956–1982, 2010.

[46] K. Lee and Y. Bresler, “Admira: Atomic decomposition for minimum rank approximation,” *IEEE Transactions on Information Theory*, vol. 56, no. 9, pp. 4402–4416, 2009.

[47] A. Beck and M. Teboulle, “A fast iterative shrinkage-thresholding algorithm for linear inverse problems,” *Siam Journal on Imaging Sciences*, vol. 2, no. 1, pp. 183–202, 2009.

[48] Rockafellar and R. Tyrrell, “Monotone operators and the proximal point algorithm,” *Siam Journal on Control and Optimization*, vol. 14, no. 5, pp. 877–0, 1976.

[49] M. V. Afonso, J. M. Bioucas-Dias, and M. A. T. Figueiredo, “An augmented lagrangian approach to the constrained optimization formulation of imaging inverse problems,” *IEEE Trans Image Process*, vol. 20, no. 3, pp. 681–695, 2011.

[50] C. A. Metzler, A. Maleki, and R. G. Baraniuk, “From denoising to compressed sensing,” *IEEE Transactions on Information Theory*, vol. 62, no. 9, pp. 5117–5144, 2016.

[51] S. V. Venkatakrishnan, C. A. Bouman, and B. Wohlberg, “Plug-and-play priors for model based reconstruction,” in *2013 IEEE Global Conference on Signal and Information Processing*, 2013, pp. 945–948.

[52] J. Zhang and B. Ghanem, “ISTA-Net: Interpretable optimization-inspired deep network for image compres-

sive sensing,” in *The IEEE Conference on Computer Vision and Pattern Recognition (CVPR)*, June 2018, pp. 1828–1837.

[53] D. O. Walsh, A. F. Gmitro, and M. W. Marcellin, “Adaptive reconstruction of phased array MR imagery,” *Magnetic Resonance in Medicine*, vol. 43, no. 5, pp. 682–690, 2000.

[54] Y. LeCun, Y. Bengio, and G. Hinton, “Deep learning,” *Nature*, vol. 521, no. 7553, pp. 436–444, 2015.

[55] K. He, X. Zhang, S. Ren, and J. Sun, “Delving deep into rectifiers: Surpassing human-level performance on imagenet classification,” *Proceedings of the IEEE International Conference on Computer Vision*, pp. 1026–1034, 2015.

[56] X. Glorot, A. Bordes, and Y. Bengio, “Deep sparse rectifier neural networks,” *Proceedings of The Fourteenth International Conference on Artificial Intelligence and Statistics*, pp. 315–323, 2011.

[57] M. D. Zeiler, “ADADELTA: an adaptive learning rate method,” *arXiv preprint arXiv:1212.5701*, 2012.

[58] D. P. Kingma and J. Ba, “Adam: A method for stochastic optimization,” *arXiv preprint arXiv:1412.6980*, 2014.

[59] M. Abadi, P. Barham, J. Chen, Z. Chen, A. Davis, J. Dean, M. Devin, S. Ghemawat, G. Irving, M. Isard *et al.*, “Tensorflow: a system for large-scale machine learning,” *OSDI*, vol. 16, pp. 265–283, 2016.

[60] Z. Wang, A. C. Bovik, H. R. Sheikh, and E. P. Simoncelli, “Image quality assessment: from error visibility to structural similarity,” *IEEE Transactions on Image Processing*, vol. 13, no. 4, pp. 600–612, 2004.